Check for updates

ORIGINAL ARTICLE

Kathleen Lyons · Raúl Bayoán Cal · Jennifer A. Franck

Effects of wavelength on vortex structure and turbulence kinetic energy transfer of flow over undulated cylinders

Received: 31 December 2022 / Accepted: 2 June 2023 © The Author(s), under exclusive licence to Springer-Verlag GmbH Germany, part of Springer Nature 2023

Abstract Passive flow control is commonly used on bluff bodies for drag and oscillating lift reduction across a range of engineering applications. This research explores a spanwise undulated cylinder inspired by seal whiskers that is shown to reduce hydrodynamic forces when compared to smooth cylinders. Although the fluid flow over this complex geometry has been documented experimentally and computationally, investigations surrounding geometric modifications to the undulation topography have been limited, and fluid mechanisms by which force reduction is induced have not been fully examined. Five variations of undulation wavelength are simulated at Reynolds number Re = 250 and compared with results from a smooth elliptical cylinder. Vortex structures and turbulence kinetic energy (TKE) transfer in the wake are analyzed to explain how undulation wavelength affects force reduction. Modifications to the undulation wavelength generate a variety of flow patterns including alternating vortex rollers and hairpin vortices. Maximum force reduction is observed at wavelengths that are large enough to allow hairpin vortices to develop without intersecting each other and small enough to prevent the generation of additional alternating flow structures. The differences in flow structures modify the magnitude and location of TKE production and dissipation due to changes in mean and fluctuating strain. Decreased TKE production and increased dissipation in the near wake result in overall lower TKE and force reduction. Understanding the flow physics linking geometry to force reduction will guide appropriate parameter selection in bio-inspired design applications.

Keywords Seal whisker · Wavy cylinder · Passive flow control · Vortex dominated flows · Wake dynamics

1 Introduction

Reduction of drag and oscillating lift forces from flow over a bluff body is desirable in many engineering applications to conserve energy, reduce material costs, and lower fatigue-induced stresses on a structure. Toward this goal, various passive flow control methods have been implemented such as the addition of surface roughness, ridges, and helical strakes to an otherwise smooth surface [1,2], in many instances designed for a

Communicated by Ashok Gopalarathnam.

K. Lyons · J. A. Franck (⋈)

Department of Engineering Physics, University of Wisconsin-Madison, Madison, WI, USA

E-mail: jafranck@wisc.edu

K. Lyons

E-mail: lyons6@wisc.edu

R. B. Cal

Department of Mechanical and Materials Engineering, Portland State University, Portland, OR, USA

E-mail: rcal@pdx.edu

Published online: 18 June 2023

specific application. Another potential solution is a bio-inspired design from the unique undulated geometry of seal whiskers, which are shown to dramatically reduce drag and oscillating lift forces when compared to a smooth cylinder [3–5]. This research focuses on the vortex structures and turbulent mechanisms within the wake of the seal whisker-inspired undulated cylinder and examines the influence of undulation wavelength on force reduction.

Understanding the flow over a smooth circular cylinder and geometric modifications continues to be important [6-12]. Disruptions to the geometry along the spanwise direction can break up the nominally two-dimensional wake structures that are primarily responsible for large force fluctuations [2]. In their computational work, Zhang et al. [1] compared several shape-modified circular cylinders with passive flow control including ridged, O-ringed, linear wavy, and sinusoidal wavy cylinders at Re = 5000. Only the linear wavy and sinusoidal wavy cylinders appreciably reduced lift and drag forces, and they hypothesized that the wavy cylinder topography modified the free shear layers and stabilized the wake.

The wavy cylinder geometry is defined by a diameter that varies sinusoidally between a maximum and minimum value along the spanwise direction at a specific wavelength. Using dye visualization and pressure measurements, Ahmed and Bays-Muchmore [13] demonstrated three-dimensional boundary layer separation lines and the roll-up of the boundary layer into streamwise vortices near locations of maximum diameter. They measured a reduction in mean drag for four wavy cylinder models as compared with a smooth circular cylinder. Zhang et al. [14] found that the wavy cylinder geometry produced overall lower turbulence kinetic energy (TKE) levels in the near wake which contributed to drag reduction; however, individual transport terms were not examined. Lam and Lin [15] investigated the flow over the wavy cylinder geometry for a range of wavelength and amplitude variations demonstrating a nonlinear trend of forces with respect to wavelength and two locations of minimum drag. They classified the flow into three regimes with respect to wavelength using spanwise vorticity to characterize three-dimensional flow structure distortion and vortex formation length. Similar to Ahmed and Bays-Muchmore [13], at wavelengths where forces were minimal, they hypothesized that the introduction of additional streamwise vorticity tended to stabilize the two-dimensional spanwise vorticity of the free shear layers and thus prevent roll-up [15].

Another common three-dimensional modification to cylinders is the addition of helical strakes, which has been shown to reduce vortex shedding coherence and prevent frequency lock-in [16]. An extension of this variation is the helically twisted elliptical cylinder formed by rotating an elliptical cross section along the spanwise direction. This geometry has been shown to reduce drag when compared to smooth and wavy cylinders [17,18] and displays a nonlinear drag versus wavelength trend similar to that seen by Lam and Lin [15]. Kim et al. [18] noted that minimal drag and oscillating lift forces were seen at wavelengths where vortex shedding is suppressed.

The complex spanwise undulations of a seal whisker and the resulting reduced oscillatory response is likely responsible for the ability of seals to track prey via hydrodynamic trail following [19–21]. The whiskers are sensitive to disturbances in the water as they have been shown to minimize vortex-induced-vibration (VIV) when compared to smooth cylinders, resulting in a larger signal-to-noise ratio [3,22,23]. Hanke et al. [3] showed that flow over the harbor seal whisker geometry resulted in a 40% reduction in average drag and 90% reduction in oscillating lift forces compared with a smooth cylinder at Re = 500. Given these qualities, the undulated seal whisker has inspired biomimetic designs such as flow sensors [23,24] and turbine blades [25,26] among others.

However, the seal whisker geometry has greater complexity than the previously mentioned passive control surfaces due to out-of-phase surface undulations along both the streamwise and transverse directions. Experiments employing real seal whiskers have shown vibrations over a broad range of frequencies when subjected to disturbances in the incoming flow [27]. PIV in the wake of real elephant seal whiskers displayed faster wake recovery for flow over the undulated whisker versus a smooth whisker [28]. The specific geometry and parameters generated by Hanke et al. [3] are widely used in fluid flow investigations, with only a handful of papers exploring geometry modifications, or examining how changing the undulation parameters affects the forces and/or resulting wake structures. Simulations by Witte et al. [4] compared the undulated topography with two different wavelengths and found no change in drag but considerable reduction in root-mean-square (RMS) lift for the higher wavelength model. Hans et al. [5] simulated flow over various models with and without undulations and concluded that optimal force reduction was achieved with the inclusion of undulations along both the thickness and chord length. A 90-degree offset between the pair of undulations produced the required secondary vortex structures to stabilize the shear layer as reported by Liu et al. [29] and further supported by Yoon et al. [30].

Due to the complexity of the geometry, previous investigations have primarily focused on demonstration of drag and oscillating lift reduction and addressed the impact of a limited number of modifications. While Hans et al. [5] simulated four models, Yoon et al. [30] simulated seven. Both investigations demonstrated the importance of undulations in the chord and thickness directions. Liu et al. [29] simulated a larger collection of models by modifying both the amplitude and wavelength; however, the two undulation amplitude values were dependent on one another. Work by Lyons et al. [31] was the first to systematically investigate each of the geometric parameters by redefining them independent from one another and simulating 16 modified feature combinations. Lyons et al. [31] identified the most important geometric parameters as the aspect ratio, the two undulation amplitudes, and the undulation wavelength. The significant importance of the aspect ratio is expected as the effect of modifying the thickness-to-chord ratio of an ellipse has been extensively studied [32–34]. The interplay between the two undulation amplitudes of the whisker-inspired geometry and their modification was described by Yuasa et al. [35]; however, wavelength has yet to be thoroughly investigated.

This paper varies undulation wavelength utilizing detailed computations and assesses the impact on the forces and wake structures through a TKE analysis. The analysis of TKE has been previously used to provide a comparison between experimental results and turbulent theory [6], explore improvements in turbulence modeling [36,37], and clarify underlying physics of complex flow structures [38]. While the correlation between lower TKE in the near wake and reduced forces on the body has been well established for bluff body flows [14,30,39,40], the fundamental processes by which the various geometries lead to lower TKE (and hence force reduction) are not well understood. This work investigates the flow physics to provide a link between geometric topography, specifically undulation wavelength, and force reduction through detailed simulations of the undulated cylinder. A deeper understanding of how geometric effects influence this complex flow will progress the development of whisker-inspired design for passive flow control and biomimetic sensing applications.

Section 2 introduces the computational methods and the whisker-inspired model. The force results, instantaneous flow structures, and turbulence terms are compared and discussed in Sect. 3, and the summary and conclusions are presented in Sect. 4.

2 Numerical methods

2.1 Flow simulation details

Direct numerical simulation (DNS) of the flow over the undulated cylinder is performed using the open-source finite-volume libraries, *OpenFOAM* [41]. The governing equations are the incompressible Navier–Stokes and continuity equations,

$$\frac{\partial u_i}{\partial t} + \frac{\partial u_i u_j}{\partial x_j} = -\frac{1}{\rho} \frac{\partial p}{\partial x_i} + \nu \frac{\partial^2 u_i}{\partial x_j \partial x_j} \tag{1}$$

$$\frac{\partial u_j}{\partial x_j} = 0, \tag{2}$$

where p is pressure, ν is kinematic viscosity, ρ is density, and u_j represents each of the three instantaneous velocity components. The OpenFOAM libraries implement a second-order accurate finite-volume scheme with Gaussian integration and linear cell center to cell face interpolation. The matrix equations are solved using a generalized geometric-algebraic multi-grid method with Gauss-Seidel smoothing. The pressure-implicit split-operator (PISO) algorithm is used for pressure-velocity coupling, and time stepping is completed using a second-order accurate backward scheme. The timestep size is allowed to vary while maintaining a Courant-Friedrichs-Lewy number less than one, with an average timestep of 0.02 convective time units.

The computational domain is sketched in Fig. 1 where a uniform freestream velocity U_{∞} in the x-direction and zero pressure gradient conditions are applied at the inlet, and no-slip conditions are enforced on the model wall. At the outlet boundary, fixed pressure and zero velocity gradient conditions are imposed. The domain has a radius of 75T, where T is the average thickness, and two wavelengths are modeled for each geometry in the spanwise direction which is shown to be sufficient for resolving three-dimensional effects in the wake of seal whisker topographies [42]. Spanwise periodicity is enforced with cyclic boundary conditions that are applied to the front and back x-y planes of the domain; thus, tip effects are not modeled. Each model is oriented at

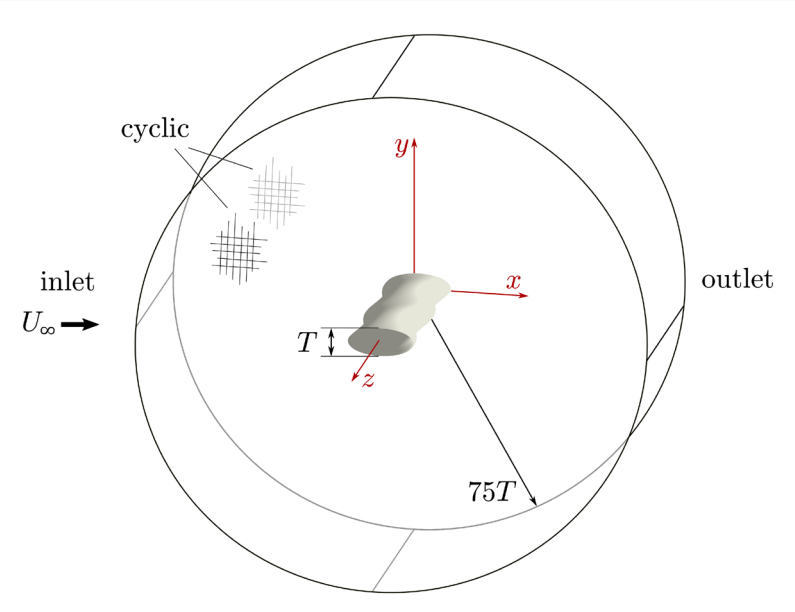


Fig. 1 Computational domain is shown (not to scale) with a radius of 75T and a two-wavelength periodic span. Model is oriented at zero angle of attack, and uniform velocity is in the positive x-direction

zero angle of attack with respect to the chord length such that the time-averaged lift coefficient is negligible. Simulations are completed at Re = 250, where Re is based on average thickness, Re = $U_{\infty}T/\nu$. The choice of Re is driven by biological relevance, motivated by real-life seal foraging speed and whisker thickness [43]. Furthermore, the low Re enables the use of DNS for flow simulation with a highly resolved mesh and clear visualization of flow structures. It is noted that the flow over the smooth ellipse remains in a nominally laminar periodic vortex shedding regime. The introduction of three-dimensional instabilities during the transition to turbulence for flow over a smooth circular cylinder may begin at Re < 200 [9,44], but the elliptical shape may shift the onset of instabilities to a higher Re.

2.2 Calculation of turbulence kinetic energy

To understand the flow mechanisms responsible for the variations between models, an analysis of the turbulence kinetic energy budget is performed. To begin the analysis, the Reynolds decomposition

$$\boldsymbol{u}(x, y, z, t) = \overline{\boldsymbol{U}}(x, y, z) + \boldsymbol{u}'(x, y, z, t), \tag{3}$$

where overline represents a time-averaged quantity and prime represents a fluctuating quantity, is applied to the momentum equation to derive the Reynolds stress equation [45]. Due to the geometric variation across span, no averaging is done across the spatial directions. Half of the trace of the Reynolds stress tensor represents the turbulence kinetic energy

$$k = \frac{1}{2}\overline{u_i'u_i'},\tag{4}$$

and its transport can be written in the form used by Pope [45] as

$$\underbrace{\overline{U_{j}} \frac{\partial k}{\partial x_{j}}}_{\mathcal{C}} + \underbrace{\frac{1}{2} \frac{\partial}{\partial x_{j}} \overline{u'_{i} u'_{i} u'_{j}}}_{T^{(c)}} + \underbrace{\frac{1}{\rho} \frac{\partial}{\partial x_{j}} \overline{u'_{j} p'}}_{T^{(p)}} - \underbrace{2v \frac{\partial}{\partial x_{j}} \overline{u'_{i} S'_{ij}}}_{T^{(v)}} = \underbrace{-\overline{u'_{i} u'_{j}} \frac{\partial \overline{U_{i}}}{\partial x_{j}}}_{\mathcal{C}} - \underbrace{2v \overline{S'_{ij} S'_{ij}}}_{\mathcal{C}}$$
convection
$$\underbrace{T^{(p)}}_{T^{(p)}} \qquad \underbrace{T^{(v)}}_{T^{(v)}} \qquad \underbrace{\mathcal{P}}_{T^{(v)}}_{T^{(v)}} \qquad \underbrace{Viscous}_{T^{(v)}}_{T^{(v)}}$$
convection
$$\underbrace{T^{(v)}}_{T^{(v)}} \qquad \underbrace{T^{(v)}}_{T^{(v)}} \qquad \underbrace{T^{(v)}}_{T^{$$

where p' is the fluctuating pressure, and S'_{ij} is the fluctuating strain rate tensor $S'_{ij} = \frac{1}{2} \left(\frac{\partial u'_i}{\partial x_j} + \frac{\partial u'_j}{\partial x_i} \right)$. The three-dimensional nature of the flow requires that each term in Eq. 5 be summed over indices j = 1, 2, and 3.

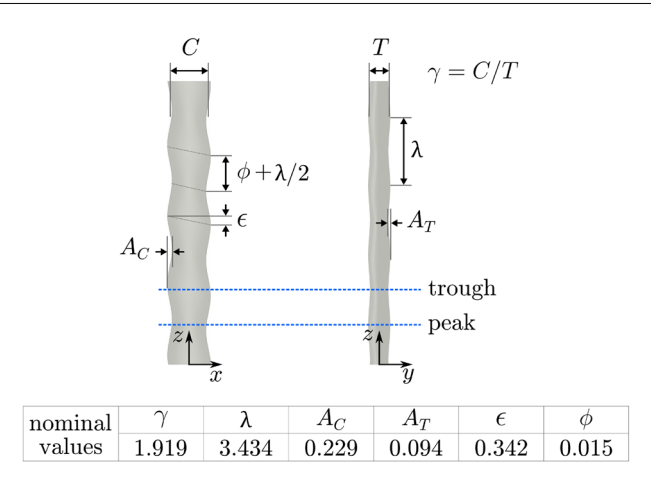


Fig. 2 Top and side view of the seal whisker model with nondimensional geometric parameters identified

2.3 Model description

The baseline whisker model is constructed using the geometric framework and dimensions presented by Hanke et al. [3]. There is variation in whisker dimensions within the harbor seal species (*Phoca vitulina*) and at the individual level. Published average measurements also deviate slightly from one another as discussed in the review by Zheng et al. [46]. While measurements have been reported by several sources including Hanke et al. [3], Ginter et al. [47], Rinehart et al. [48], and Murphy et al. [49], the model and measurements presented by Hanke et al. comprised of average dimensions obtained through photogrammetry of 13 whiskers which remains one of the standard representations of harbor seal whisker geometry [4,5,30,50]. However, this model does not enable easy examination of geometric modifications as the defined dimensions are coupled with one another. Therefore, the model parameters are redefined in terms of hydrodynamic relevance and nondimensionalized to allow each parameter to be varied independently of one another. Descriptions of the model parameters are detailed by Lyons et al. [31].

Figure 2 displays the seal whisker geometry with average chord length C, average thickness T, and undulation amplitudes in the chord and thickness, A_C and A_T , respectively. The periodicity of the topography is governed by the wavelength (λ) and is further perturbed by the undulation asymmetry (ϕ) and offset (ϵ) parameters. The nominal values for the baseline harbor seal model presented by Hanke et al. [3] are listed at the bottom of Fig. 2. The chord length and thickness are combined to form the aspect ratio (γ) , and amplitudes A_C and A_T are nondimensionalized by the average thickness T, while ϕ and ϵ are nondimensionalized by wavelength. A detailed description of the conversion of geometric parameters from the definition proposed by Hanke et al. [3] is included in work by Lyons et al. [31]. In Fig. 2, the spanwise locations of maximum and minimum thickness amplitude are marked with dotted lines and referred to hereafter as peak and trough, respectively.

To investigate the effect of wavelength, five different wavelength seal whisker-inspired geometries are simulated and compared with a smooth elliptical cylinder of the same aspect ratio. The baseline model with $\lambda=3.43$ is simulated, along with two models with lower wavelength, $\lambda=1$ and $\lambda=2$, and two models with higher wavelength, $\lambda=5$ and $\lambda=6.86$. The top view of each model is shown in Fig. 3 with its associated wavelength value. The other five nondimensional parameters are held constant across the models.

2.4 Computational flow parameters

The drag and lift force coefficients for each geometry are calculated to gain an understanding of the overall trends in force reduction. Drag and lift coefficients are calculated from the drag force F_D and lift force F_L as

$$C_{\rm D} = \frac{2F_{\rm D}}{\rho U_{\infty}^2 T L_{\rm z}} \tag{6}$$

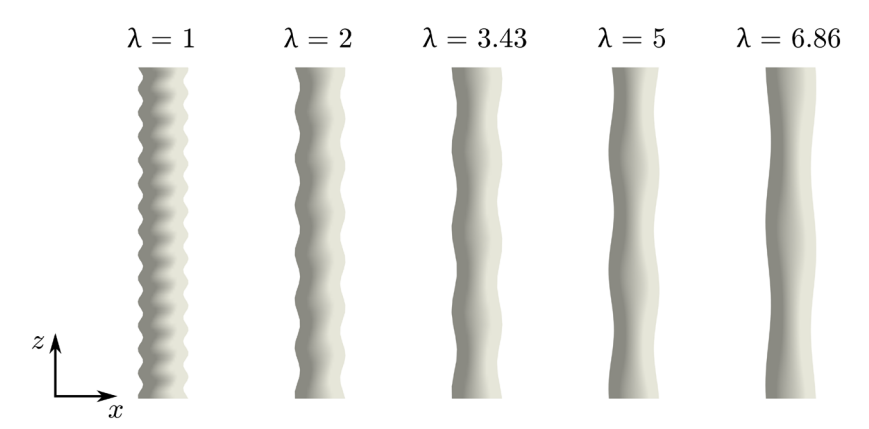


Fig. 3 Top view of whisker-inspired models

$$C_{\rm L} = \frac{2F_{\rm L}}{\rho U_{\infty}^2 C L_{\rm z}} \,. \tag{7}$$

The drag and lift coefficients are normalized by the average frontal area, TL_z , and average planform area, CL_z , respectively, where L_z is the whisker span. The lack of camber in all models produces a nominally zero value for the time-averaged C_L , and thus, the root-mean-square value, $C_{L,RMS}$, is used for analysis. The lift force frequency f is nondimensionalized as

$$f^* = \frac{fT}{U_{\infty}}. (8)$$

The Strouhal number St is defined as the dominant nondimensional frequency of the lift force spectrum. Calculation of the mean velocity $\overline{U_j}$ and mean pressure fields is computed over 600 nondimensional convective time units, $t^* = tU_{\infty}/T$. Spatial derivatives are calculated within *OpenFOAM* on the original computational mesh. Fluctuating components are calculated for 301 unique time instances spanning $30t^*$ (equivalent to between 4.4 and 7.7 shedding cycles depending on the model). The use of $30t^*$ is determined to be sufficiently large to achieve convergence of time-averaged fluctuating terms. A negligible difference is seen between calculations using $20t^*$ and $30t^*$ for the $\lambda = 3.43$ case. After calculation, all fields are sampled onto a coarser three-dimensional Cartesian grid (resolution of $\Delta x = \Delta y = \Delta z = 0.1T$) to enable further post-processing and imported into *MATLAB* where terms are time-averaged and visualized.

3 Results and discussion

3.1 Effect of wavelength on forces and flow structures

The plot of $\overline{C_D}$ and $C_{L,RMS}$ values in Fig. 4 illustrates the considerable range of oscillating lift and drag forces that result from wavelength variation. Values for the smooth elliptical cylinder are shown as dashed and dotted lines on the figure. The baseline seal whisker geometry ($\lambda = 3.43$) has 10% lower drag and 96% lower RMS lift than the ellipse. A similar reduction in bulk force has been noted by others [3,4,42]. When $\lambda = 1$, the force values are quite similar to those of the smooth ellipse even though other geometric modifications are present. However, the $\overline{C_D}$ value is slightly higher for this case than for the smooth ellipse, indicating that the introduction of undulations alone does not reduce drag, but undulation wavelength is important as well.

As wavelength increases to $\lambda = 3.43$, C_D and $C_{L,RMS}$ decrease. At higher wavelengths, $\lambda = 5$ and $\lambda = 6.86$, $C_{L,RMS}$ increases slightly, while $\overline{C_D}$ reaches its minimum at $\lambda = 5$. Witte et al. [4] also simulated a whisker variation with a twice-nominal wavelength ($\lambda = 6.86$), and their results show similar drag but lower oscillating lift forces. The discrepancy may be due to setting the undulation offset ϵ to zero in their models. The trend of lift and drag forces with respect to wavelength shown in Fig. 4 is similar to the nonlinearity seen for wavy cylinder wavelength variations [15] and helically twisted elliptical cylinders [18].

As a complement to the bulk force values, Fig. 5 displays contours of time-averaged streamwise velocity $\overline{U_x}/U_\infty$ at peak and trough cross sections for each model. Flow variations are solely due to changes in the

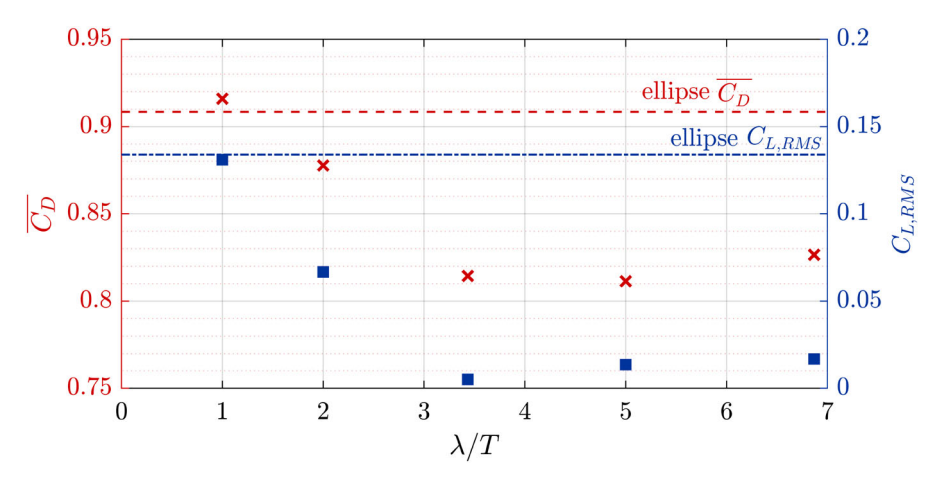


Fig. 4 Time-averaged drag and RMS lift values presented for each wavelength model. For models with $\lambda > 2$, there is a significant reduction in both $\overline{C_D}$ and $C_{L,RMS}$ when compared with the smooth ellipse. Both $\overline{C_D}$ and $C_{L,RMS}$ sharply decrease to minima at $\lambda = 5$ and $\lambda = 3.43$, respectively, before increasing again

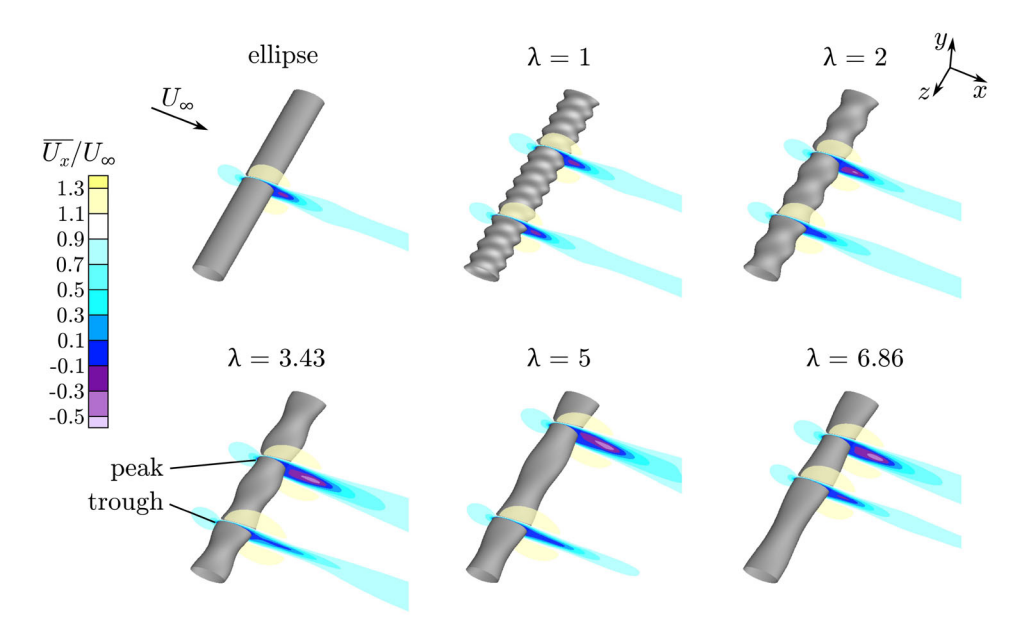


Fig. 5 Contours of mean streamwise velocity display the variation within the recirculation region as a function of wavelength. Contours are displayed at a representative peak and trough cross section for each model

frequency of undulation, as the geometric cross sections at the respective peaks and troughs are identical. The peak and trough velocity profiles for the $\lambda=1$ case are similar to those of the smooth ellipse as might be expected from the similarity in forces. Both cross sections of the $\lambda=2$ case display a longer recirculation length than the ellipse and $\lambda=1$ models, and the peak cross section has a larger area of reversed flow, while flow behind the trough cross section is nominally in the positive x-direction. The $\lambda=3.43, 5$, and 6.86 cases have a larger variation between their peak and trough cross sections. For each, the trough cross section has minimal flow reversal indicating a reduction in shear layer roll-up.

The variation in the mean velocity profiles indicates that changes in undulation frequency cause differences in the flow pattern. To visualize flow structures, isosurfaces of nondimensional Q are plotted in Fig. 6 and colored by z-vorticity with red indicating positive and blue indicating negative vorticity. The shed structures behind the $\lambda=1$ and 2 models are similar to a typical von Kármán vortex street. However, the $\lambda=1$ model produces nominally two-dimensional vortices, whereas flow over the $\lambda=2$ model includes additional waviness in the spanwise vortex rolls, and braid-like structures form between rolls. These three-dimensional braid-like structures are created as streamwise and transverse vorticity develops. Secondary vorticity develops naturally

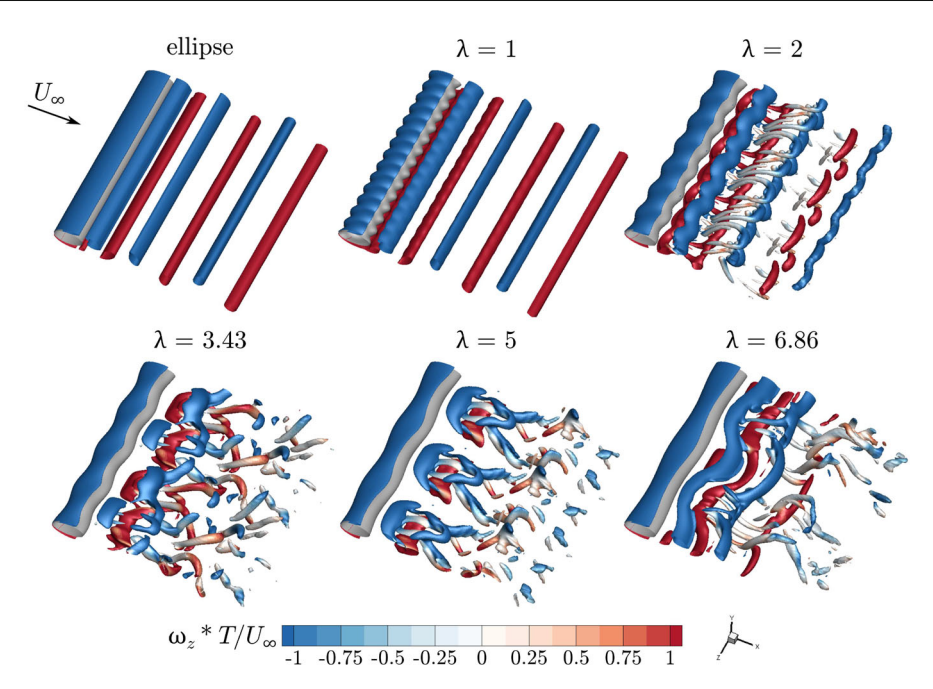


Fig. 6 Isosurfaces of nondimensional Q=0.3 colored by spanwise vorticity illustrate the effect of wavelength modification on flow structure patterns. Flow over the ellipse and $\lambda=1$ are primarily two-dimensional, while the $\lambda=2$ model generates secondary streamwise and transverse vorticity, and hairpin vortices are visible at larger wavelengths

in the flow behind smooth circular cylinders as a result of deformation of primary vortex cores leading to mode-A instability [8,9,51,52]. However, the secondary structures observed for the $\lambda=2$ model are initiated by the increased spanwise velocity induced by the undulations of the model and are more closely spaced along the span than three to four diameters as typically seen for mode-A [52].

In the wake of a smooth circular cylinder at similar Re, it is common for the flow to develop vortex dislocations along the spanwise length in addition to the mode-A instability [53,54]. These intermittent occurrences lead to a break in the periodicity of the mode-A instability and typically cause a large decrease in the drag force time history [44]. Examination of force data indicates no such intermittent variations for any of the whisker-inspired models at this Re. Flow over the $\lambda = 3.43$ and $\lambda = 5$ models is periodic in time as shown by the lift force and is three-dimensional with hairpin vortex structures developing in the wake. The $\lambda = 5$ case develops vortex structures that are shed in tandem along the span. However, the structures behind $\lambda = 3.43$ alternate shedding from top and bottom at 180 degrees of phase for each wavelength section along the span resulting in a near-zero instantaneous C_L as upper and lower forces work to negate one another. For both of these cases, the undulations are spaced far enough apart that the spanwise coherent vortex structures do not interfere with one another as they develop and convect downstream. The wavy cylinder geometry also displays three-dimensional flow structure distortion due to changes in wavelength [14,15]. At wavelengths where forces were minimal, Lam and Lin [15] hypothesize that the introduction of additional streamwise vorticity tends to stabilize the two-dimensional spanwise vorticity of the free shear layers and thus prevent roll-up. At the highest wavelength examined, the $\lambda = 6.86$ case contains a combination of patterns. Hairpin-like features are visible downstream of peak cross sections, while largely two-dimensional roller-type structures appear downstream of the trough. The larger distance between undulations, and subsequently between hairpin structures, enables the development of additional vortex rollers. In contrast, the close spanwise spacing of the hairpin vortices in the $\lambda = 3.43$ and 5 cases prevents shear layer roll-up behind trough regions of the geometry.

3.2 Analysis of turbulence kinetic energy

The instantaneous flow structures illustrated by isosurfaces of Q-criterion offer insight into the development and transfer of TKE. Isosurfaces of Q for $\lambda = 3.43$ are repeated in Fig. 7 (gray) and superimposed with isosurfaces of instantaneous turbulence kinetic energy,

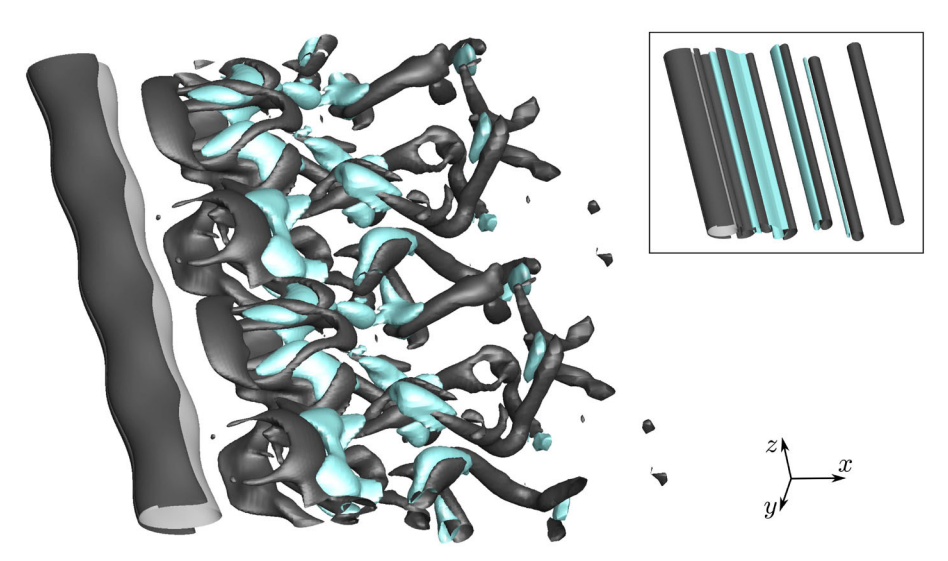


Fig. 7 Isosurfaces of nondimensional Q = 0.3 shown in gray and instantaneous turbulence kinetic energy k' = 0.08 in blue for the $\lambda = 3.43$ case highlight the link between vortex flow structures and TKE. For comparison, the ellipse case is displayed in the upper right with isosurface values of nondimensional Q = 0.3 in gray and k' = 0.12 in blue (color figure online)

$$k' = \frac{1}{2} u_i' u_i', (9)$$

shown in blue. A moderate k' isosurface level is chosen in order to depict structures which envelope regions of higher k'. The k' isosurfaces are interlaced with those of Q and convect downstream with the vortex structure. Regions of large k' form as shear is generated between vortices of different rotation, enabling energy transfer from the mean flow to the fluctuating quantities. In the upper right of Fig. 7, isosurfaces of nondimensional Q and k' in the wake of a smooth ellipse are displayed for comparison.

As energy is transferred from the mean flow into TKE, inspection of TKE contours allows for a more detailed comparison between models. The top row in Fig. 8 displays contours of TKE in the x-z plane at y=0. The cases $\lambda=2$, 3.43, and 6.86 are chosen to illustrate the effects representative of a small, medium, and large wavelength as the $\lambda=1$ case has been shown to exhibit characteristics most similar to a smooth elliptical cylinder. In each case, the largest values of TKE appear periodically along the span with a frequency dependent on the undulation wavelength. Maximum TKE values occur downstream of the recirculation region, and thus, the location of maximum TKE is further downstream for the $\lambda=3.43$ and $\lambda=6.86$ cases than for $\lambda=2$, mirroring the pattern seen in the elongation of the recirculation lengths in Fig. 5. Furthermore, the maximum magnitude of TKE is noticeably lower for these larger wavelength models. The lower TKE values in the near wake correlate with lower $\overline{C_D}$ and $C_{L,RMS}$ as indicated in Fig. 4. This is consistent with the direct relationship between TKE and lift and drag forces previously noted by Yoon et al. [30] and Chu et al. [39] for whisker-inspired geometries and by Lin et al. [40] and Zhang et al. [14] for wavy cylinders.

The bottom two rows in Fig. 8 contain x-y cross sections at trough and peak locations. The cross-sectional views show the maximum TKE values for $\lambda=3.43$ and $\lambda=6.86$ occur neither at the trough nor peak cross section, but rather in between, a pattern also noted by Yoon et al. [30]. Conversely, the $\lambda=2$ case contains a maximum behind the trough cross section, similar to wavy cylinders of similar wavelength where TKE maxima appear and streamwise velocity recovers more quickly behind node locations [14]. The introduction of hairpin vortex structures at wavelengths larger than 2 may initiate the spanwise shift of the TKE maxima as the shear layer is more stable at trough locations for these geometries.

While force trends and general flow structures largely agree with those previously investigated for whisker-inspired geometries [3,4,42], wavy cylinders [14,15], and helically twisted elliptical cylinders [18], calculation and analysis of TKE transport terms for flow over a seal whisker geometry are completed in the next sections for the first time to the authors' knowledge. The relationship among the TKE transport terms with respect to downstream development is illustrated in Fig. 9. To gain an understanding of the overall transport trend with respect to the streamwise direction alone, the TKE equation terms are averaged over a full wavelength span from $\lambda/2$ to $3\lambda/2$ and averaged over a domain of y/T=0 to 2. While it is recognized that some asymmetry exists across the y-axis, a single side was chosen for calculation in order to capture dominant structures and

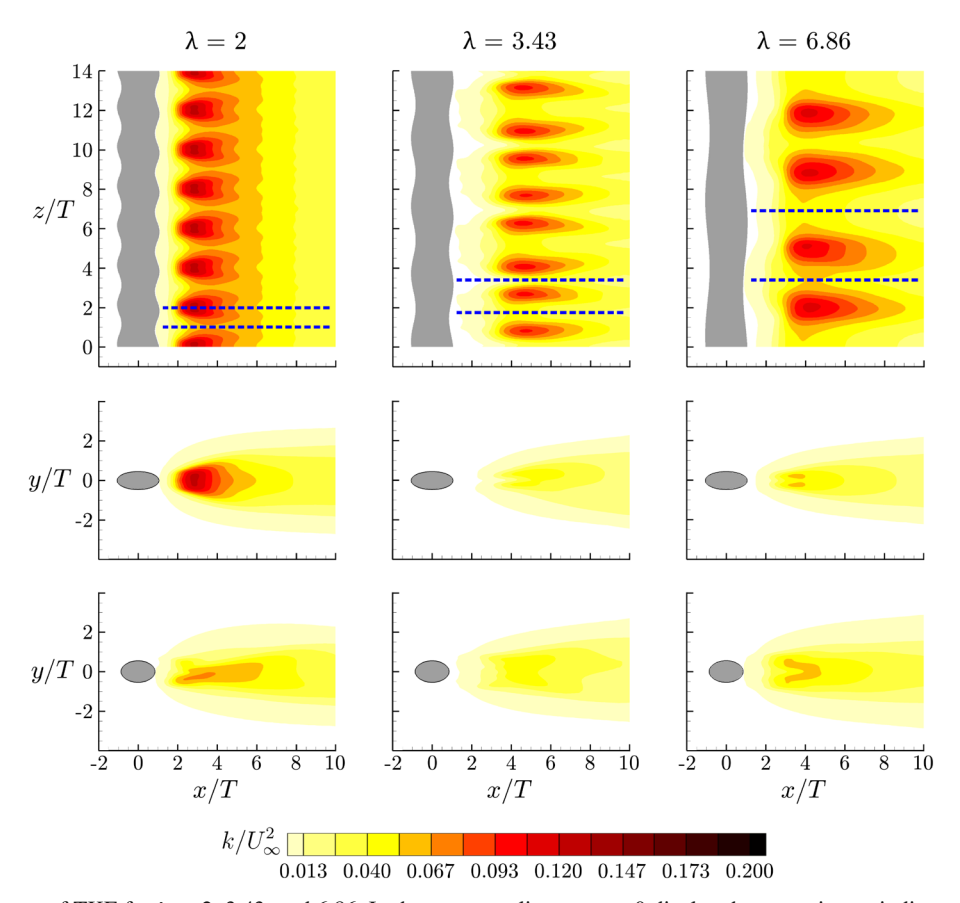


Fig. 8 Contours of TKE for $\lambda = 2$, 3.43, and 6.86. In the top row, slices at y = 0 display the spanwise periodic pattern of TKE and dashed lines are shown at trough and peak locations. Slices in the x-y plane at trough and peak locations, in rows two and three, respectively, highlight the difference in TKE due to undulation wavelength

prevent TKE terms located at positive and negative y locations from canceling one another. The three plots are normalized by the maximum average production for each associated case to allow for easier comparison. The turbulent transport terms, $T^{(c)}$, $T^{(p)}$, and $T^{(v)}$, are represented by the dashed green lines, while mean convection, \mathcal{C} , is designated by a solid red line, mean production, \mathcal{P} , is shown in blue, and mean dissipation, ε , is shown in purple. The peak average production shifts further downstream for the larger wavelength models. Likewise, peak values for \mathcal{C} and $T^{(p)}$ occur further downstream for $\lambda = 3.43$ and 6.86.

Peak $T^{(p)}$ values appear within the average recirculation region for each model, a typical location for similar geometries such as a circular cylinder [37]. Immediately downstream of the body, \mathcal{P} is negative indicating that the average flow in this region is dominated by reversed flow and TKE is transferred back to the mean flow. For the $\lambda=2$ case, peak $T^{(p)}$ occurs at the downstream location where \mathcal{P} first crosses zero. In comparison, the $T^{(p)}$ curve reaches its peak further downstream after \mathcal{P} is already positive for the $\lambda=3.43$ and 6.86 geometries. At its peak, \mathcal{P} is balanced predominately by mean convection, dissipation, and pressure transport. While the magnitude of mean convection is similar for all three cases, the proportion of $T^{(p)}$ and ε varies. The ratio $T^{(p)}/\varepsilon$ for $\lambda=2$ and 6.86 is 0.82 and 0.75, respectively, whereas the ratio for $\lambda=3.43$ is much lower at 0.34. The lower ratio for the 3.43 case indicates the tendency for the flow to dissipate turbulence in this region rather than redistribute it via fluctuating pressure. A decrease in pressure fluctuations, especially in the near wake, has implications for reduction of flow noise.

A detailed understanding of the effects of wavelength variation on the production and dissipation terms can be gained by examining them individually. The production term, $\mathcal{P} = -\overline{u_i'u_j'}\left(\partial\overline{U_i}/\partial x_j\right)$, in the TKE transport equation represents the energy converted from mean kinetic energy into TKE through mean shear interaction with Reynolds stresses. In this way, TKE provides a connection between the mean and turbulent quantities. The location and magnitude of \mathcal{P} are dependent on the mean shear and turbulent fluctuations induced by near wake flow structures.

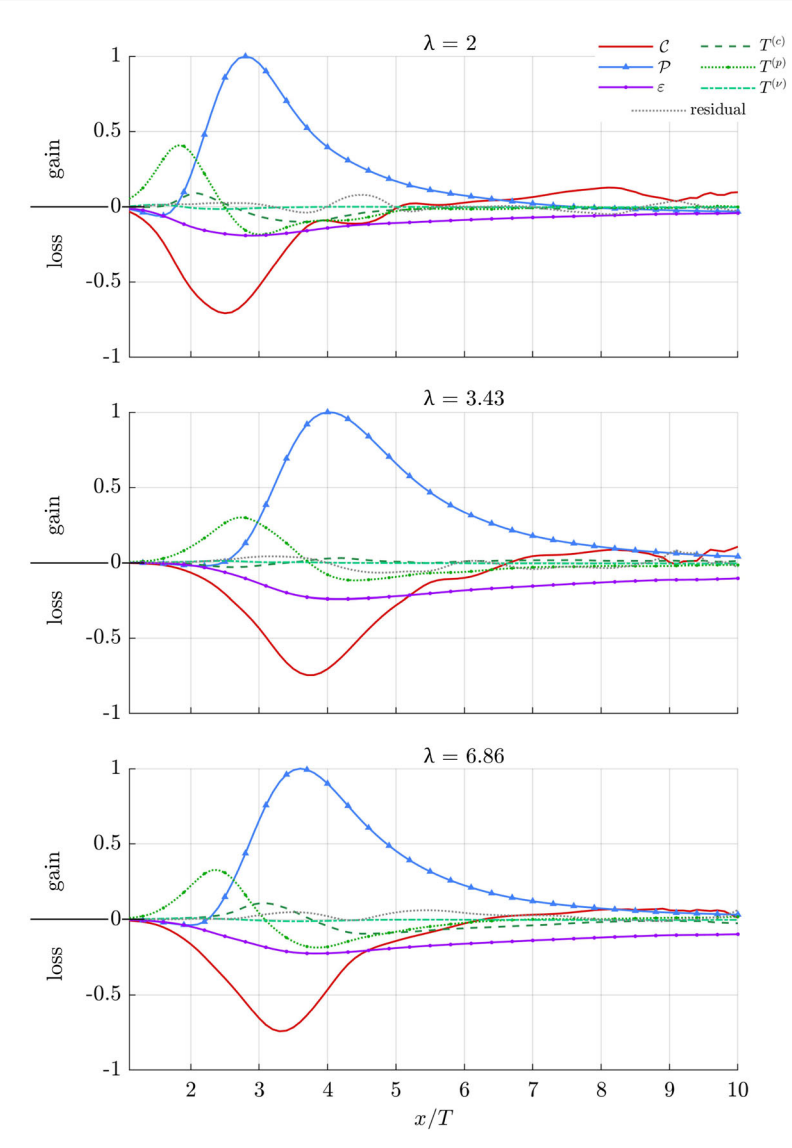


Fig. 9 Budgets of TKE transport are presented with respect to downstream location. Values are span-averaged and averaged in the y-direction from y/T = 0 to 2

In order to compare the models of varying wavelength, the production terms at the wake centerline y/T=0 are span-averaged and are displayed in Fig. 10. Similar to the force behavior, the $\lambda=1$ model closely follows the ellipse production trend line. For the $\lambda=2$ geometry, the peak production occurs further downstream and with a lower maximum value. The flow over $\lambda=3.43$ and 5 has yet lower peak production values with occurrence further downstream. Finally, the $\lambda=6.86$ flow reverses the decreasing trend with slightly larger peak production occurring earlier than $\lambda=3.43$.

The spanwise variation of the wake centerline production is illustrated in the bottom portion of Fig. 10 by the blue shading for $\lambda=2,3.43$, and 6.86, while the solid line represents the same span-averaged values as in the upper figure. The variation with respect to spanwise position provides a more detailed picture of the production than the span-averaged curves that reduce the flow to one dimension. The peak production for $\lambda=2$ occurs earlier than the other two cases and with considerably less variation. Centerline production for $\lambda=3.43$ has the largest variation with local zero values possible even as the span-average reaches its peak. Both $\lambda=3.43$ and 6.86 have considerable variability 3T downstream of peak production, while downstream production from the $\lambda=2$ case remains nominally zero.

As shown in Fig. 9, one of the primary transport mechanisms in the near wake region is the turbulent pressure transport $T^{(p)}$, which redistributes energy among the TKE equation terms. The span-averaged pressure

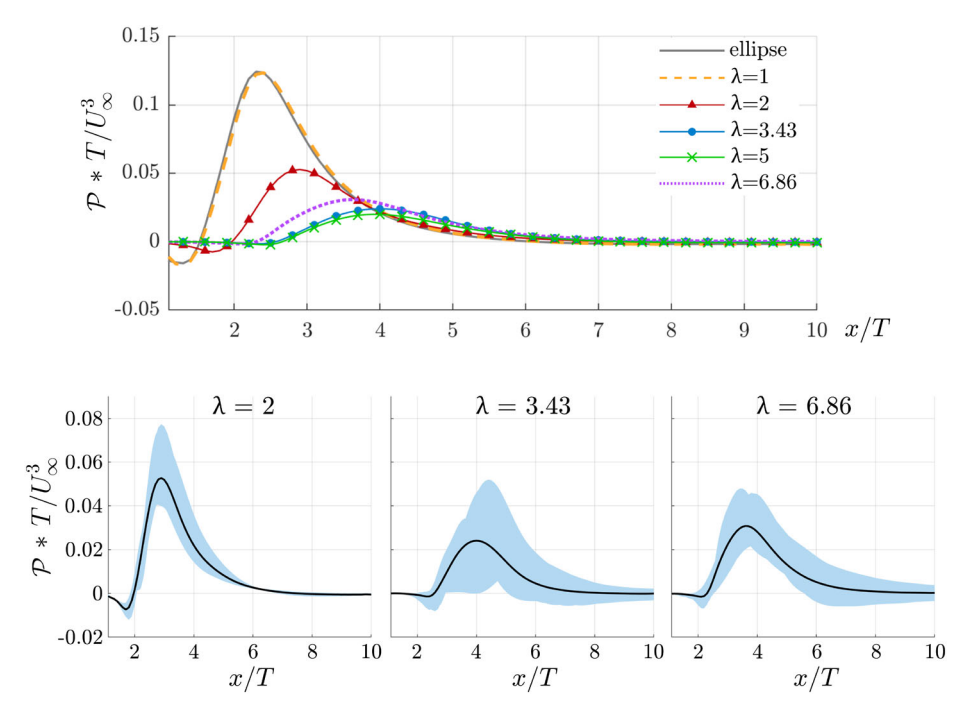


Fig. 10 Span-averaged curves of TKE production are shown along the wake centerline y/T = 0. Below, spanwise variation of wake centerline production values is shaded in blue with the span-averaged quantity shown as a solid line (color figure online)

transport values are plotted with respect to downstream location at y/T=0 in Fig. 11. For $\lambda>2$, the overall magnitude of the span-averaged pressure transport is considerably reduced compared to the large peak present in the elliptical cylinder case. In the lower portion of the figure, the spanwise variation is shaded in blue. While span-averaged values are minimal, the variation along the span is substantial, indicating the importance of local three-dimensional effects. Larger wavelengths ($\lambda=3.43$ and 6.86) extend the range of these spanwise effects further downstream as indicated by the larger variation for x/T>4 compared to the small variation seen for the $\lambda=2$ case.

In primary opposition to \mathcal{P} , removal of TKE is accomplished predominantly through viscous dissipation, $\varepsilon = 2\nu \overline{S'_{ij}S'_{ij}}$, at the smallest length scales. Governed by the fluctuating strain rate, dissipation is largest where fluctuating terms are located. Not all cases achieve peak dissipation along the wake centerline y/T=0, nevertheless, the span-averaged wake centerline dissipation values provide ease of comparison and are plotted in Fig. 12. Both $\lambda=2$ and 3.43 have large dissipation peaks although the $\lambda=2$ peak occurs closer to the body. In contrast, $\lambda=5$ and 6.86 have broad, flat peaks between x/T=3 and 5 rather than a sharp peak as seen for $\lambda=2$ and 3.43.

Spanwise variation of centerline dissipation is shown by the blue shading in the lower portion of Fig. 12 where the solid black line is the span-averaged value. Although $\lambda=2$ and 3.43 have peak span-averaged centerline dissipation values of similar magnitude, there is little spanwise variation in $\lambda=2$, whereas the $\lambda=3.43$ flow has a wide range of dissipation values and considerable dissipation at further downstream locations (x/T>6). The wake of $\lambda=6.86$ maintains dissipation variation downstream as well, but to a lesser extent. Both the lower level of TKE production and the higher amount of dissipation contribute to the $\lambda=3.43$ flow having the lowest levels of TKE compared to the other wavelengths.

3.3 Turbulence kinetic energy spanwise effects

Insight into the relationship between flow structure and \mathcal{P} is gained by extracting a y-z contour slice at the location of peak span-averaged production along the wake centerline y/T=0, profiles of which are shown in Fig. 10. Figure 13a displays contours of \mathcal{P} at x/T=2.9, 4, and 3.6 for the $\lambda=2$, 3.43, and 6.86 flows, respectively. The shapes of the contours mimic the shapes of the vortical structures shown in Fig. 6 with the largest values of \mathcal{P} occurring near the edges of the vortex structures where mean shear interacts with Reynolds

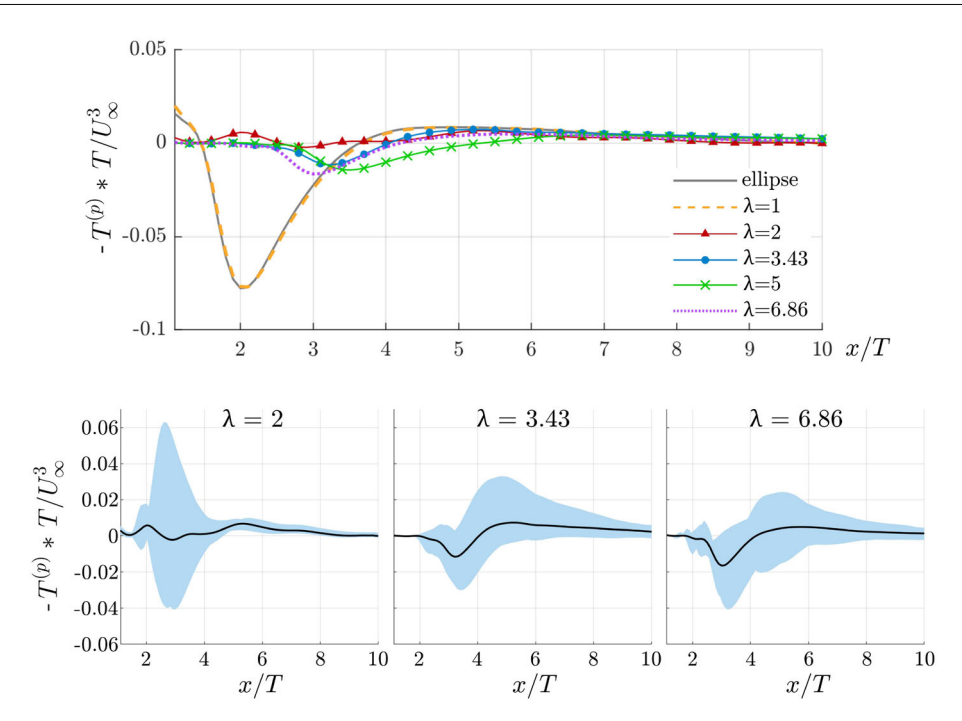


Fig. 11 Span-averaged values of pressure transport are plotted along the wake centerline y/T = 0. Below, spanwise variation of wake centerline pressure transport values are shaded in blue with the span-averaged quantity shown as a solid line

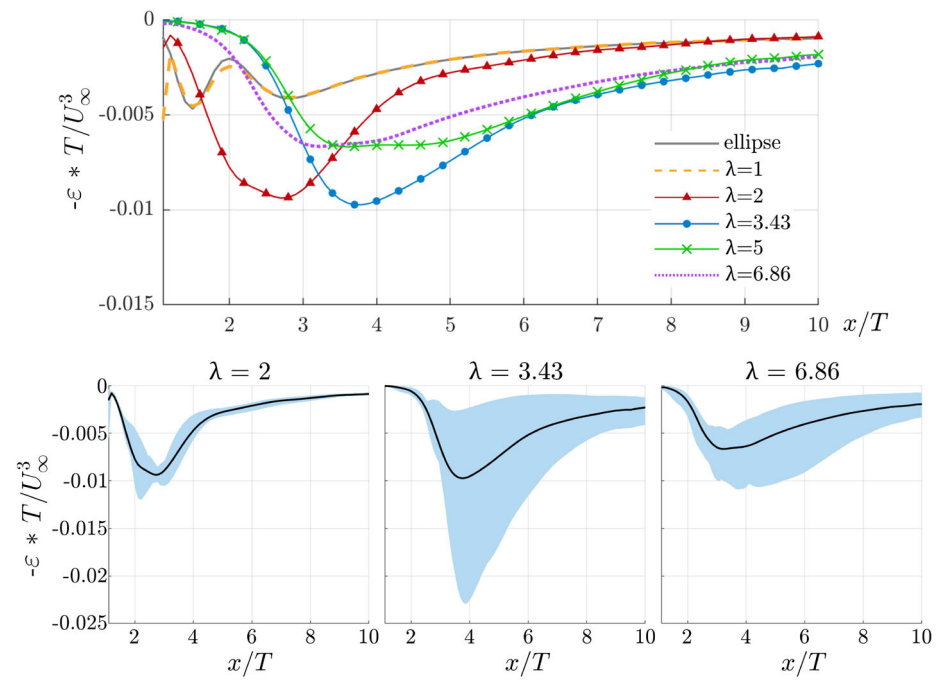


Fig. 12 Span-averaged values of TKE dissipation are displayed along the wake centerline y/T = 0. Below, spanwise variation of wake centerline dissipation values is shaded in blue with the span-averaged quantity shown as a solid line

stresses. The wavy nature of the vortex rolls produced in the wake of $\lambda=2$ is visible in the periodic hot spot pattern of the $\mathcal P$ contours, and the coherent hairpin structures that develop behind the $\lambda=3.43$ case create two distinguishable $\mathcal P$ patches centered at $z/T=\lambda/2$ and $3\lambda/2$. In this case, the two patches are separated with a small region of near-zero production occurring around $z/T=\lambda$. The combination of flow structures that develop behind the $\lambda=6.86$ geometry is apparent in the $\mathcal P$ contour pattern as well. Patches of production

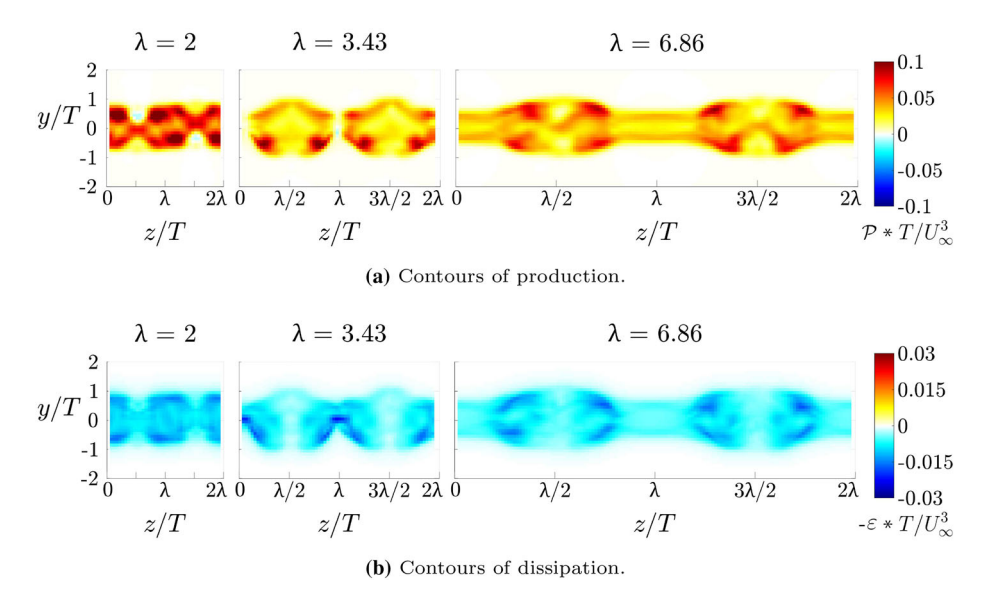


Fig. 13 Contours of production and dissipation in the y-z plane are displayed at locations of maximum span-averaged production (as displayed in Fig. 10), x/T = 2.9, 4, and 3.6 for the $\lambda = 2$, 3.43, and 6.86 models, respectively

due to hairpin-like structures form near $z/T=\lambda/2$ and $3\lambda/2$, similar to the $\lambda=3.43$ case. However, a stripe pattern on either side of these patches appears resulting from the additional vortex rollers that appear at this wavelength. The combination of flow structures ultimately results in a higher overall level of $\mathcal P$ for the larger wavelength case than for $\lambda=3.43$ where secondary roller structures are suppressed. Likewise, large values of turbulent pressure transport are a result of the product of velocity and pressure fluctuations. Locations of large $T^{(p)}$ magnitude align generally with areas of high production and are not displayed here.

Contour slices of $-\varepsilon$ in the y-z plane are taken at the same downstream locations and displayed in Fig. 13b. The overall dominant shapes are similar to those of \mathcal{P} as they both are linked to the underlying vortex structure; however, there are several notable differences. While both production and dissipation occur at locations where turbulent fluctuations are large, production of TKE requires mean strain while dissipation relies on fluctuating strain rates. Larger \mathcal{P} values are located near shear layers, especially apparent by the horizontal stripe pattern shown in Fig. 13a for the $\lambda=6.86$ case, whereas dissipation is more dispersed around the edges of vortex structures. Furthermore, the $\lambda=3.43$ case develops a large dissipative sink between the two shed structures at $z/T=\lambda$, and although space exists between the shed hairpin-like structures of the $\lambda=6.86$ case, a similar TKE sink is not found.

Viewing the production and dissipation contours in the y-z plane also displays the asymmetry with respect to y that occurs for the $\lambda=3.43$ flow. Larger \mathcal{P} and $-\varepsilon$ values are located at negative y, while placement is more uniform for other wavelength models. It is possible that shed vortex structure with the inclusion of the hairpin vortex allows for increased stability in this orientation and Re.

To examine the complexity of spanwise effects on TKE, the TKE budget along the wake centerline y/T=0 is shown as a function of spanwise position in Fig. 14 for $\lambda=2$, 3.43, and 6.86 at a downstream location of peak span-averaged production. Corresponding to the structures shown in Fig. 13a, all three cases have local minima near $z/T=\lambda$. While the production term for the $\lambda=2$ and 6.86 models decreases moderately at $z/T=\lambda$, it diminishes to near zero around λ for the $\lambda=3.43$ case as the proximity of the coherent hairpin structures prevents the development of oscillating vortex shedding in between. While dissipation remains relatively constant over the span for $\lambda=2$ and 6.86, it displays a maximum magnitude at $z/T=\lambda$ for the $\lambda=3.43$ case. Complementing production and dissipation, the remaining TKE terms are responsible for transport, of which the turbulent transport terms contribute more than mean convection. For $\lambda=2$, the turbulent pressure transport $T^{(p)}$ is largely balanced by turbulent convection $T^{(c)}$ near $z/T=\lambda$. The appearance of $T^{(c)}$ correlates with the higher $C_{\rm L,RMS}$ value that manifests for the $\lambda=2$ case. For the three cases shown, the viscous diffusion term $T^{(v)}$ is generally small, but interestingly becomes a dominant term near $z/T=\lambda$ in the $\lambda=3.43$ case.

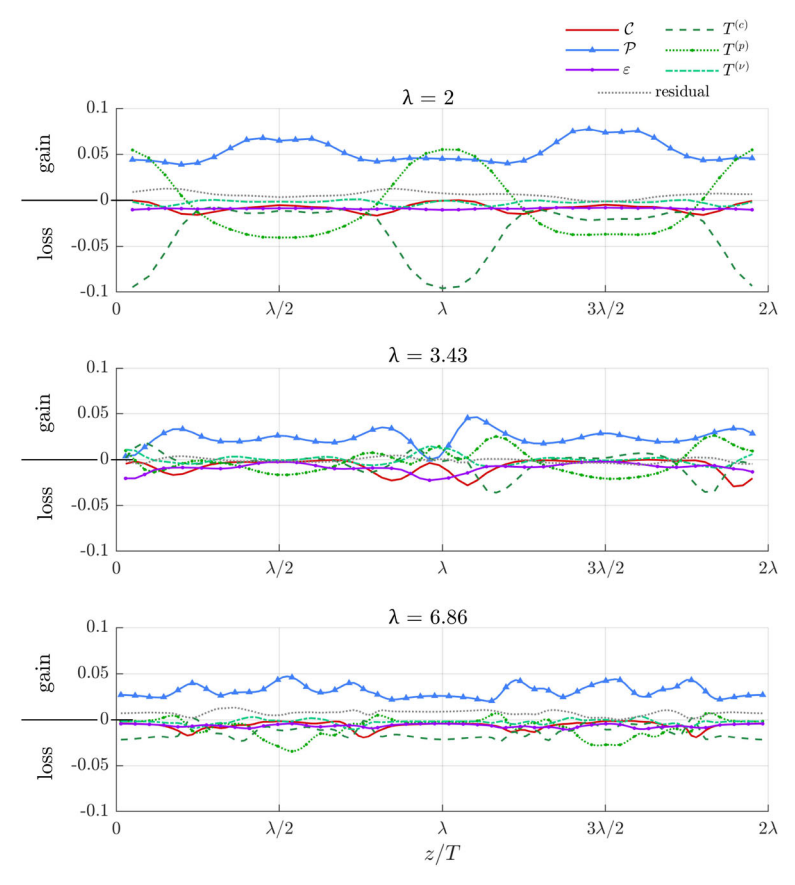


Fig. 14 Spanwise budgets of TKE transport are shown along the wake centerline y/T = 0 for $\lambda = 2$, 3.43, and 6.86 cases at peak production downstream locations x/T = 2.9, 4, and 3.6, respectively

4 Conclusions

Flow over five seal whisker-inspired geometries with various undulation wavelengths is simulated and compared with a smooth elliptical cylinder at Re = 250. An analysis of TKE transport terms is performed to explore the underlying mechanisms linking flow structures, TKE values, and force reduction. The drag and oscillating lift are significantly reduced for undulated geometries, with the $\lambda = 3.43$ case achieving a reduction of 96% in $C_{\rm L,RMS}$ and 10% in $\overline{C_{\rm D}}$, agreeing with trends in prior research.

Furthermore, modification of undulation wavelength gives rise to a variety of flow patterns with hairpin vortex structures forming for models with $\lambda > 2$, replacing the two-dimensional von Kármán vortex street of smaller wavelengths. The resulting three-dimensional flow structures influence the creation of mean shear and Re stresses which, in turn, impact the magnitude and location of TKE production and dissipation. Topographies that minimize alternating vortex shedding create an elongated recirculation region and move the location of maximum TKE production further downstream. Analysis of TKE transport terms demonstrates that TKE in the near wake region is dominated by production and dissipation, while turbulent pressure redistributes the energy among the terms.

Although these trends are seen at multiple wavelengths, they are most amplified for the $\lambda=3.43$ model, which generates hairpin vortices with spanwise spacing such that they do not interfere with one another, yet are close enough to prevent additional shear layer roll-up in between. Such structures both decrease TKE production and create space for a TKE sink between vortices, decreasing overall TKE in the near wake and corresponding forces on the body. At the downstream location of maximum production, this model generates a wake where turbulent fluctuations are more likely to dissipate rather than redistribute TKE as shown by the low value of the ratio $T^{(p)}/\varepsilon$. For the $\lambda=3.43$ case, $T^{(p)}/\varepsilon=0.34$, while $\lambda=2$ and 6.86 have ratios closer to unity at 0.82 and 0.75, respectively. In summary, the vortex structures both lower the TKE production and increase the dissipation allowing for a lower overall level of TKE compared to the other wavelength models.

Understanding the impact of wavelength modification on vortex structure and the subsequent effects on specific TKE terms provides a guide for the selection of bio-inspired geometry parameters. Within the values investigated, it is shown that the nominal bio-inspired wavelength of $\lambda=3.43$ is optimal for drag and VIV reduction, but there are also force reduction properties of higher wavelength values. While this work concentrates on variations in wavelength, further investigation would explore the effects of other geometric parameters and extend to higher Re, which would be important to generalize these findings toward broader engineering applications.

Acknowledgements The authors kindly thank Dr. Christin Murphy for her guidance, knowledge, and insight into biological systems. This research was conducted using computational resources provided by the Center for Computation and Visualization at Brown University and the US Department of Defense HPC Modernization Program.

Authors' contributions KL and JAF were responsible for conceptualization. All authors assisted with the development of methodology. KL completed analysis and created the initial draft manuscript. All authors assisted with revisions and editing.

Funding This work was supported by the National Science Foundation (J.A.F. and K.L., grant number CBET-2035789), (R.B.C., grant number CBET-2037582) under program manager Ron Joslin.

Availability of data and materials Data sets are available upon request.

Declarations

Conflict of interest The authors report no conflict of interest.

Ethical approval Not applicable.

Appendix A: Mesh resolution study

Generating a high-quality, structured mesh surrounding the whisker models is time-intensive and complex given the three-dimensional undulations. An improved method is introduced by Yuasa et al. [35] that utilizes a smooth mesh morphing algorithm coupled to the flow solver. Geometric parameters are specified and obtained through an analytical expression of the whisker surface topography to actively morph from one geometric realization to the next. In addition to the time savings in meshing, the method presented by Yuasa et al. ensures repeatable realizations of the geometry by defining the surface topography with a complete analytical expression. For the following simulations, an initial three-dimensional structured mesh is generated for a smooth ellipse of the same aspect ratio and span as the desired model. The flow over the smooth elliptical cylinder is computed for 100 nondimensional convective time units, $t^* = tU_{\infty}/T$, while the flow structures in the wake are developed. Then over the next five t^* , the mesh is morphed into the desired topography. The flow is given another $95t^*$ to fully transition before flow field statics are collected for the next $600t^*$.

A comparison of mesh resolution results at Re = 500 for the baseline λ = 3.43 model is shown in Table 1. While analysis is completed at Re = 250, the mesh resolution is validated at the higher Reynolds number Re = 500 to compare with data from prior literature. The table shows the value for $\overline{C_D}$ decreases slightly with increasing mesh size and converges to three decimal places for the two largest meshes. Similarly, St remains constant for the three largest meshes. To compare performance in the wake, contours of TKE are plotted for the 4.14M cell and 6.14M cell meshes in Fig. 15. Slices at y = 0 are displayed in the top row showing comparable contour patterns and magnitudes. The dotted lines designate the locations of the trough

Table 1 Table includes the tested mesh resolutions for $\lambda = 3.43$ case at Re = 500 with the number of nodes in the spanwise (N_z) , azimuthal (N_θ) , and radial (N_r) directions, the uniform spanwise spacing $(\Delta z/T)$, and the minimum radial spacing $(\Delta r/T_{\min})$

$N_{ m total}$	N_{z}	$N_{ heta}$	$N_{ m r}$	$\Delta z/T$	$\Delta r/T_{ m min}$	$\overline{C_{ m D}}$	St
1.01M	110	100	94	0.063	0.005	0.706	0.15
2.06M	140	130	115	0.049	0.004	0.704	0.17
4.14M	170	160	154	0.041	0.003	0.696	0.17
6.14M	215	176	164	0.032	0.002	0.696	0.17

The 4.14 M cell mesh is selected for use in further analysis

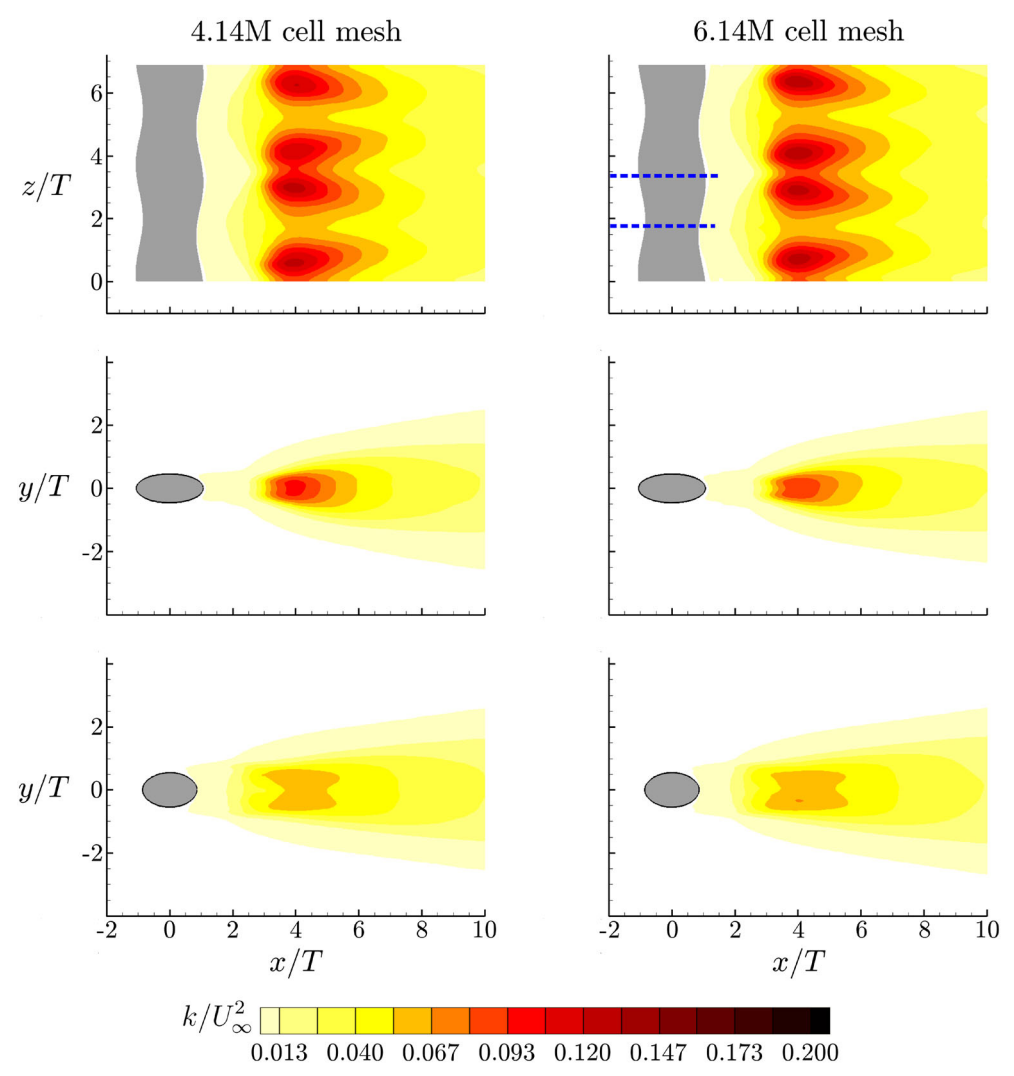
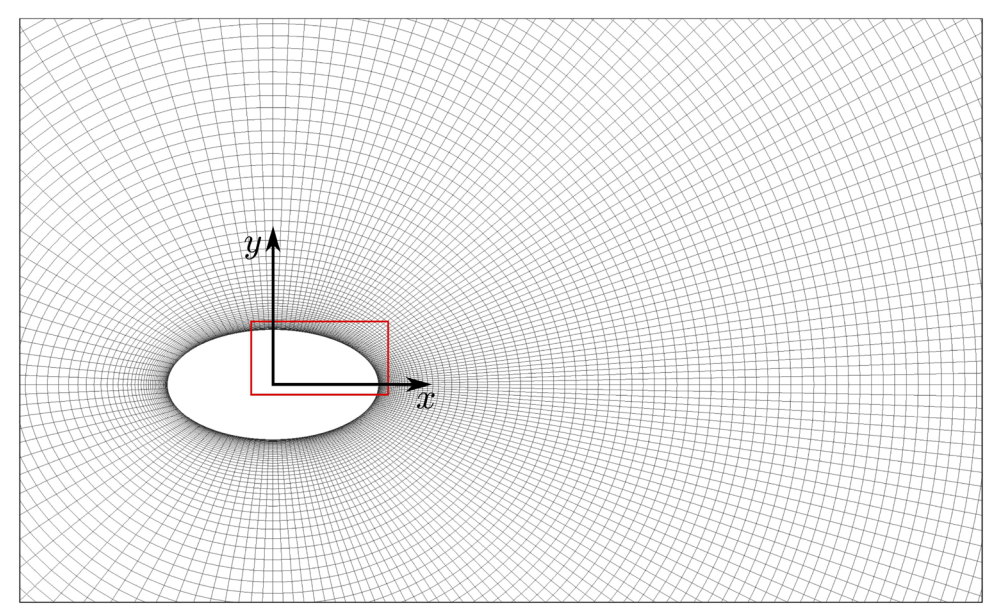


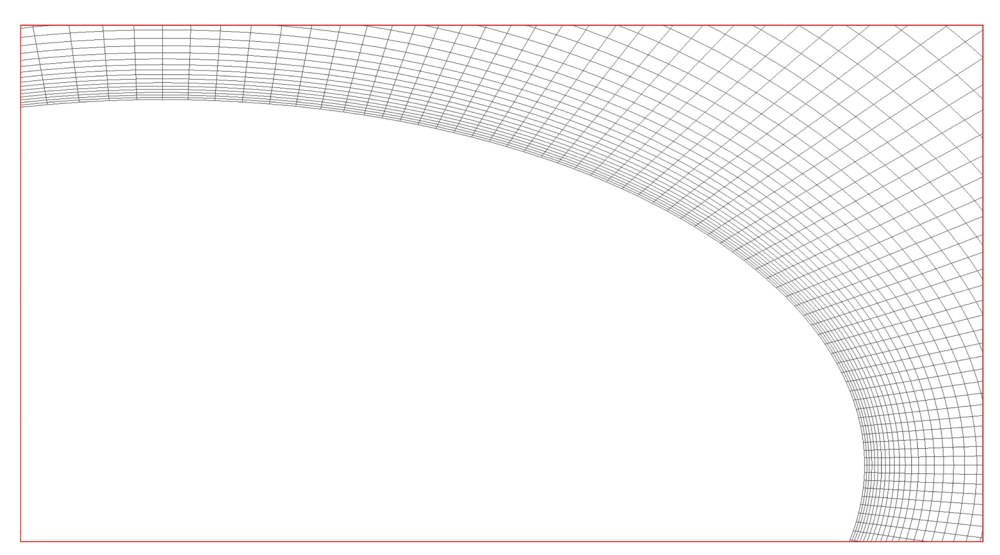
Fig. 15 Contours of TKE for the chosen mesh with 4.14M cells and a larger mesh with 6.14M cells show comparable results. The top row displays slices at y = 0. Below, contours at trough and peak cross sections are shown

and peak cross sections shown in the second and third rows, respectively. Slight differences can be seen in the x-y cross-section contours at downstream locations ($x \gtrsim 4T$). The 4.14M cell mesh is chosen for analysis as further increases in mesh size show negligible differences.

The mesh for the $\lambda = 3.43$ is shown in Fig. 16a with an inset view of the near wall region in Fig. 16b. As wavelength is changed for each model, the whisker length is modified to maintain a two-wavelength spanwise domain. The number of mesh cells in the spanwise direction is adjusted accordingly for each model, while the azimuthal and radial resolution is maintained.



(a) Resolution in near wake region



(b) Zoomed view of figure A2a inset

Fig. 16 Mesh for $\lambda = 3.43$ case contains 4.14 M cells and provides adequate resolution near the wall and in the wake

References

- 1. Zhang, K., Katsuchi, H., Zhou, D., Yamada, H., Han, Z.: Numerical study on the effect of shape modification to the flow around circular cylinders. J. Wind Eng. Ind. Aerodyn. 152, 23–40 (2016). https://doi.org/10.1016/j.jweia.2016.02.008
- Choi, H., Jeon, W.P., Kim, J.: Control of flow over a bluff body. Annu. Rev. Fluid Mech. 40, 113–139 (2008). https://doi. org/10.1146/annurev.fluid.39.050905.110149
- 3. Hanke, W., Witte, M., Miersch, L., Brede, M., Oeffner, J., Michael, M., et al.: Harbor seal vibrissa morphology suppresses vortex-induced vibrations. J. Exp. Biol. 213(15), 2665–2672 (2010). https://doi.org/10.1242/jeb.043216
- 4. Witte, M., Hanke, W., Wieskotten, S., Miersch, L., Brede, M., Dehnhardt, G., et al.: On the wake flow dynamics behind harbor seal vibrissae—a fluid mechanical explanation for an extraordinary capability. In: Tropea, C., Bleckmann, H. (eds.) Results of the DFG Priority Programme 1207 "Nature-inspired Fluid Mechanics" 2006–2012, pp. 271–289. Springer, Berlin (2012). https://doi.org/10.1007/978-3-642-28302-4_17
- 5. Hans, H., Miao, J., Weymouth, G., Triantafyllou, M.: Whisker-like geometries and their force reduction properties. In: MTS/IEEE OCEANS—Bergen. Norway 2013 1–7 (2013)
- Townsend, A.A.: Momentum and energy diffusion in the turbulent wake of a cylinder. Proc. R. Soc. Lond. A 197(1048), 124–140 (1949). https://doi.org/10.1098/rspa.1949.0054

- Bloor, M.S., Gerrard, J.H.: Measurements on turbulent vortices in a cylinder wake. Proc. R. Soc. Lond. A 294(1438), 319–342 (1966)
- Roshko, A.: Perspectives on bluff body aerodynamics. J. Wind Eng. Ind. Aerodyn. 49(1), 79–100 (1993). https://doi.org/10. 1016/0167-6105(93)90007-B
- Williamson, C.H.K.: Vortex dynamics in the cylinder wake. Annu. Rev. Fluid Mech. 28(1), 477–539 (1996). https://doi.org/ 10.1146/annurev.fl.28.010196.002401
- Yan, F., Yang, H., Wang, L.: Study of the drag reduction characteristics of circular cylinder with dimpled surface. Water 13(2), 197 (2021). https://doi.org/10.3390/w13020197
- 11. Mao, X., Wang, B.: Spanwise localized control for drag reduction in flow passing a cylinder. J. Fluid Mech. (2021). https://doi.org/10.1017/jfm.2021.154
- Li, Z., Tang, T., Liu, Y., Arcondoulis, E.J.G., Yang, Y.: Numerical study of aerodynamic and aeroacoustic characteristics of flow over porous coated cylinders: effects of porous properties. Aerosp. Sci. Technol. 105, 106042 (2020). https://doi.org/ 10.1016/j.ast.2020.106042
- Ahmed, A., Bays-Muchmore, B.: Transverse flow over a wavy cylinder. Phys. Fluids A 4(9), 1959–1967 (1992). https://doi. org/10.1063/1.858365
- 14. Zhang, W., Daichin, Lee, S.J.: PIV measurements of the near-wake behind a sinusoidal cylinder. Exp. Fluids **38**(6), 824–832 (2005). https://doi.org/10.1007/s00348-005-0981-9
- 15. Lam, K., Lin, Y.F.: Effects of wavelength and amplitude of a wavy cylinder in cross-flow at low Reynolds numbers. J. Fluid Mech. 620, 195–220 (2009). https://doi.org/10.1017/S0022112008004217
- 16. Zhou, T., Razali, S.F.M., Hao, Z., Cheng, L.: On the study of vortex-induced vibration of a cylinder with helical strakes. J. Fluids Struct. 27(7), 903–917 (2011). https://doi.org/10.1016/j.jfluidstructs.2011.04.014
- 17. Jung, J.H., Yoon, H.S.: Large eddy simulation of flow over a twisted cylinder at a subcritical Reynolds number. J. Fluid Mech. 759, 579–611 (2014). https://doi.org/10.1017/jfm.2014.581
- 18. Kim, W., Lee, J., Choi, H.: Flow around a helically twisted elliptic cylinder. Phys. Fluids (2016). https://doi.org/10.1063/1. 4948247
- Dehnhardt, G., Mauck, B., Bleckmann, H.: Seal whiskers detect water movements. Nature 394(6690), 235–236 (1998). https://doi.org/10.1038/28303
- 20. Dehnhardt, G., Mauck, B., Hanke, W., Bleckmann, H.: Hydrodynamic trail-following in harbor seals (Phoca vitulina). Science. 293(5527), 102–104 (2001). https://doi.org/10.1126/science.1060514
- 21. Schulte-Pelkum, N., Wieskotten, S., Hanke, W., Dehnhardt, G., Mauck, B.: Tracking of biogenic hydrodynamic trails in harbour seals (*Phoca vitulina*). J. Exp. Biol. **210**(5), 781–787 (2007). https://doi.org/10.1242/jeb.02708
- 22. Miersch, L., Hanke, W., Wieskotten, S., Hanke, F.D., Oeffner, J., Leder, A., et al.: Flow sensing by pinniped whiskers. Philos. Trans.: Biol. Sci. 366(1581), 3077–3084 (2011)
- Kottapalli, A.G.P., Asadnia, M., Miao, J.M., Triantafyllou, M.S.: Harbor seal whisker inspired flow sensors to reduce vortexinduced vibrations. In: 2015 28th IEEE International Conference on Micro Electro Mechanical Systems (MEMS). p. 889–892. ISSN: 1084-6999 (2015)
- 24. Beem, H., Hildner, M., Triantafyllou, M.: Calibration and validation of a harbor seal whisker-inspired flow sensor. Smart Mater. Struct. (2013). https://doi.org/10.1088/0964-1726/22/1/014012
- 25. Shyam, V., Ameri, A., Poinsatte, P., Thurman, D., Wroblewski, A., Snyder, C.: Application of pinniped vibrissae to aeropropulsion. American Society of Mechanical Engineers Digital Collection (2015). Available from: https://asmedigitalcollection.asme.org/GT/proceedings/GT2015/56635/V02AT38A023/236853
- Ahlman, R., Flack, C., Shyam, V., Zhang, W.: Wake flow structure of a seal-whisker-inspired power turbine blade. In: AIAA Scitech 2020 Forum. American Institute of Aeronautics and Astronautics, Orlando, FL, USA (2020)
- 27. Murphy, C.T., Reichmuth, C., Eberhardt, W.C., Calhoun, B.H., Mann, D.A.: Seal whiskers vibrate over broad frequencies during hydrodynamic tracking. Sci. Rep. (2017). https://doi.org/10.1038/s41598-017-07676-w
- Bunjevac, J., Turk, J., Rinehart, A., Zhang, W.: Wake induced by an undulating elephant seal whisker. J. Visual. 21(4), 597–612 (2018). https://doi.org/10.1007/s12650-018-0484-4
- 29. Liu, G., Xue, Q., Zheng, X.: Phase-difference on seal whisker surface induces hairpin vortices in the wake to suppress force oscillation. Bioinspir. Biomim. (2019). https://doi.org/10.1088/1748-3190/ab34fe
- 30. Yoon, H.S., Nam, S.H., Kim, M.I.: Effect of the geometric features of the harbor seal vibrissa based biomimetic cylinder on the flow over a cylinder. Ocean Eng. 218, 108150 (2020). https://doi.org/10.1016/j.oceaneng.2020.108150
- 31. Lyons, K., Murphy, C.T., Franck, J.A.: Flow over seal whiskers: importance of geometric features for force and frequency response. PLoS ONE 15(10), e0241142 (2020). https://doi.org/10.1371/journal.pone.0241142
- Lindsey, W.F.: Drag of cylinders of simple shapes. National Advisory Committee for Aeronautics; NACA-TR-619. NTRS
 Author Affiliations: NTRS Report/Patent Number: NACA-TR-619 NTRS Document ID: 19930091694 NTRS Research
 Center: Legacy CDMS (CDMS). (1938). Available from: https://ntrs.nasa.gov/citations/19930091694
- Delany, N.K., Sorensen, N.E.: Low-speed drag of cylinders of various shapes. Ames Aeronautical Laboratory: National Advisory Committee for Aeronautics; NACA-TN-3038. NTRS Author Affiliations: NTRS Report/Patent Number: NACA-TN-3038 NTRS Document ID: 19930083675 NTRS Research Center: Legacy CDMS (CDMS) (1953). Available from: https://ntrs.nasa.gov/citations/19930083675
- 34. Faruquee, Z., Ting, D.S.K., Fartaj, A., Barron, R.M., Carriveau, R.: The effects of axis ratio on laminar fluid flow around an elliptical cylinder. Int. J. Heat Fluid Flow 28(5), 1178–1189 (2007). https://doi.org/10.1016/j.ijheatfluidflow.2006.11.004
- 35. Yuasa, M., Lyons, K., Franck, J.A.: Simulations of flow over a bio-inspired undulated cylinder with dynamically morphing topography. J. Fluids Struct. 111, 103567 (2022). https://doi.org/10.1016/j.jfluidstructs.2022.103567
- 36. Liu, X., Thomas, F.O.: Measurement of the turbulent kinetic energy budget of a planar wake flow in pressure gradients. Exp. Fluids 37(4), 469–482 (2004). https://doi.org/10.1007/s00348-004-0813-3
- 37. Tian, G., Xiao, Z.: New insight on large-eddy simulation of flow past a circular cylinder at subcritical Reynolds number 3900. AIP Adv. 10(8), 085321 (2020). https://doi.org/10.1063/5.0012358

- 38. Schanderl, W., Jenssen, U., Strobl, C., Manhart, M.: The structure and budget of turbulent kinetic energy in front of a wall-mounted cylinder. J. Fluid Mech. 827, 285–321 (2017). https://doi.org/10.1017/jfm.2017.486
- 39. Chu, S., Xia, C., Wang, H., Fan, Y., Yang, Z.: Three-dimensional spectral proper orthogonal decomposition analyses of the turbulent flow around a seal-vibrissa-shaped cylinder. Phys. Fluids 33(2), 025106 (2021). https://doi.org/10.1063/5.0035789
- 40. Lin, Y.F., Bai, H.L., Alam, M.M., Zhang, W.G., Lam, K.: Effects of large spanwise wavelength on the wake of a sinusoidal wavy cylinder. J. Fluids Struct. 61, 392–409 (2016), https://doi.org/10.1016/j.jfluidstructs.2015.12.004
- 41. Weller, H.G., Tabor, G., Jasak, H., Fureby, C.: A tensorial approach to computational continuum mechanics using object-oriented techniques. Comput. Phys. 12(6), 620–631 (1998). https://doi.org/10.1063/1.168744
- 42. Kim, H., Yoon, H.S.: Effect of the orientation of the harbor seal vibrissa based biomimetic cylinder on hydrodynamic forces and vortex induced frequency. AIP Adv. 10(1063/1), 5008658 (2017)
- 43. Lesage, V., Hammill, M.O., Kovacs, K.M.: Functional classification of harbor seal (*Phoca vitulina*) dives using depth profiles, swimming velocity, and an index of foraging success. Can. J. Zool. **77**(1), 74–87 (1999). https://doi.org/10.1139/z98-199
- 44. Behara, S., Mittal, S.: Wake transition in flow past a circular cylinder. Phys. Fluids **22**(11), 114104 (2010). https://doi.org/10.1063/1.3500692
- 45. Pope, S.B.: Turbulent Flows. Cambridge University Press, Cambridge (2000)
- Zheng, X., Kamat, A.M., Cao, M., Kottapalli, A.G.P.: Creating underwater vision through wavy whiskers: a review of the flow-sensing mechanisms and biomimetic potential of seal whiskers. J. R. Soc. Interface 18(183), 20210629 (2021). https:// doi.org/10.1098/rsif.2021.0629
- 47. Ginter, C.C., DeWitt, T.J., Fish, F.E., Marshall, C.D.: Fused traditional and geometric morphometrics demonstrate pinniped whisker diversity. PLoS ONE (2012). https://doi.org/10.1371/journal.pone.0034481
- Rinehart, A., Shyam, V., Zhang, W.: Characterization of seal whisker morphology: implications for whisker-inspired flow control applications. Bioinspir. Biomim. (2017). https://doi.org/10.1088/1748-3190/aa8885
- 49. Murphy, C.T., Eberhardt, W.C., Calhoun, B.H., Mann, K.A., Mann, D.A.: Effect of angle on flow-induced vibrations of pinniped vibrissae. PLoS ONE (2013). https://doi.org/10.1371/journal.pone.0069872
- 50. Wang, S., Liu, Y.: Wake dynamics behind a seal-vibrissa-shaped cylinder: a comparative study by time-resolved particle velocimetry measurements. Exp. Fluids. (2016). https://doi.org/10.1007/s00348-016-2117-9
- Leweke, T., Williamson, C.H.K.: Three-dimensional instabilities in wake transition. Eur. J. Mech. B. Fluids 17(4), 571–586 (1998). https://doi.org/10.1016/S0997-7546(98)80012-5
- 52. Williamson, C.H.K.: The existence of two stages in the transition to three-dimensionality of a cylinder wake. Phys. Fluids. 31(11):3165–3168. (1988 Nov). Publisher: American Institute of Physics. https://doi.org/10.1063/1.866925
- 53. Gerrard, J.H., Lighthill, M.J.: The wakes of cylindrical bluff bodies at low Reynolds number. Philos. Trans. R. Soc. Lond. Ser. A Math. Phys. Sci. 288(1354), 351–382 (1978). https://doi.org/10.1098/rsta.1978.0020
- 54. Williamson, C.H.K.: The natural and forced formation of spot-like 'vortex dislocations' in the transition of a wake. J. Fluid Mech. 243, 393–441 (1992). https://doi.org/10.1017/S0022112092002763

Publisher's Note Springer Nature remains neutral with regard to jurisdictional claims in published maps and institutional affiliations.

Springer Nature or its licensor (e.g. a society or other partner) holds exclusive rights to this article under a publishing agreement with the author(s) or other rightsholder(s); author self-archiving of the accepted manuscript version of this article is solely governed by the terms of such publishing agreement and applicable law.